



## Heat transfer in BCC lattice materials: Conduction, convection, and radiation



M. Shahrzadi<sup>a</sup>, M. Davazdah Emami<sup>a,\*</sup>, A.H. Akbarzadeh<sup>b,c,\*</sup>

<sup>a</sup> Department of Mechanical Engineering, Isfahan University of Technology, 84156-83111 Isfahan, Iran

<sup>b</sup> Department of Bioresource Engineering, McGill University, Montreal, QC H9X 3V9, Canada

<sup>c</sup> Department of Mechanical Engineering, McGill University, Montreal, QC H3A 0C3, Canada

### ARTICLE INFO

**Keywords:**

Heat transfer  
Open-cell foam  
BCC lattice material  
Conduction  
Convection  
Radiation

### ABSTRACT

Research studies have recently been conducted on heat transfer in architected materials. As a type of rationally-designed lightweight material, lattices have received much attention in the past few years due to their multi-functional properties, mainly realized by the application of 3D printing techniques. In the present research, fluid flow and conduction, convection, and radiation heat transfer in three-dimensional periodic BCC lattices, as a topologically cubic example among a myriad of cellular architectures, are studied for a wide range of porosity (0.7–0.99) and Reynolds numbers (1–150) via a CFD analysis. The steady and incompressible flow of cool fluid with constant thermophysical properties inside a unit cell or an assembly of unit cells is simulated using the Fluent software. First, the hydrodynamic behavior of the fluid flow in the unit cell without a thermal gradient is studied. In the absence of radiation, conduction and convection heat transfer are explored under two different thermal conditions, namely *Constant temperature at solid struts* and *Constant heat release from solid struts*. The numerical results show that cell temperature increases for the constant temperature boundary condition and decreases for the constant heat release when the cell porosity decreases at the same Reynolds number. By considering radiation mechanism via the Discrete Ordinates Method, it is observed that radiative thermal conductivity increases by increasing the porosity. The increase, linearly correlated with the cell size, slightly enhances by increasing the solid radiative emission coefficient and the applied temperature difference. At lower porosities, the heat conduction, and at higher porosities, the radiation heat transfer plays a significant role in the effective thermal conductivity. At the average cell temperature of 1800 K, the ratio of radiative thermal conductivity to the effective thermal conductivity is 95% for the porosity of 0.99 and is 12% for the porosity of 0.7. After examining all three modes of heat transfer at the constant heat release thermal condition, it is found that the temperature of solid struts increases by decreasing the Reynolds number, leading to an increase of the ratio of radiation heat transfer to the total heat transfer (the ratio rises six times as the Reynolds number decreases from 150 to 1.5625 for the porosity of 0.99). For the constant heat release thermal condition, radiation heat transfer in BCC lattices can not be ignored when the porosity is high or the thermal conductivity of constitutive solid and the flow Reynolds number are low.

### 1. Introduction

High-performance multifunctional materials are among the main design paradigms for developing next generation of optimized and smart engineering materials and structures. These materials are utilized to increase material usage efficiency, lower energy consumption, lighten the weight, and enhance the functionalities of structural elements. One of these advanced lightweight materials with unprecedented properties

is the engineered cellular solids, as a man-made counterpart of natural cellular solids found in wood, cork, bone, coral, sponge, and pumice [1–3]. Due to their unique characteristics; e.g. low density, high specific surface area, high stiffness, high permeability, and suitable energy absorption, they are widely used in various applications; for example, in heat exchangers [4–6], heat sinks [7], thermal insulators [8], medical prostheses [9] and implants [10], thermal energy storage [11], thermochemical reactors [12], energy absorption [13], solar energy systems [14], sandwich panels in aerospace [15] and transportation [16,17], and

\* Corresponding authors at: Department of Bioresource Engineering, McGill University, Montreal, QC H9X 3V9, Canada (A.H. Akbarzadeh) and Department of Mechanical Engineering, Isfahan University of Technology, 84156-83111 Isfahan, Iran (M. Davazdah Emami).

E-mail addresses: [mohsen@cc.iut.ac.ir](mailto:mohsen@cc.iut.ac.ir) (M. Davazdah Emami), [hamid.akbarzadeh@mcgill.ca](mailto:hamid.akbarzadeh@mcgill.ca) (A.H. Akbarzadeh).

Nomenclature	
A	Area [m <sup>2</sup> ]
a	Absorption coefficient [1/m]
C <sub>f</sub>	Inertia coefficient
C <sub>p</sub>	Specific heat [J/kg.K]
d <sub>p</sub>	Pore diameter [m]
d <sub>s</sub>	Strut diameter [m]
f	Friction factor
I	Radiation intensity [W/m <sup>2</sup> ]
k	Thermal conductivity [W/m.K]
k <sub>ec</sub>	Conductive thermal conductivity [W/m.K]
k <sub>eff</sub>	Effective thermal conductivity [W/m.K]
k <sub>er</sub>	Radiative thermal conductivity [W/m.K]
L	Cell size [m]
n	Reflective index
P	Pressure [N/m <sup>2</sup> ]
Q	Heat transfer [W]
q	Heat flux [W/m <sup>2</sup> ]
q̇	Heat generation [W/m <sup>3</sup> ]
Re	Reynolds number
→r	Position vector [m]
→s	Direction vector
→ṡ	Scattering direction vector
S <sub>v</sub>	Specific surface area [1/m]
T	Temperature [K]
V	Superficial velocity [m/s]
v	Local velocity [m/s]
x,y,z	Cartesian coordinate direction [m]
<i>Greek symbols</i>	
α	Darcy coefficient [kg/m <sup>3</sup> .s]
β	Non-Darcy coefficient [kg/m <sup>4</sup> ]
ε	Emissivity
κ	Permeability [m <sup>2</sup> ]
μ	Dynamic viscosity [kg/m.s]
ρ	Density [kg/m <sup>3</sup> ]
σ	Stefan-Boltzmann constant ( $5.67 \times 10^{-8}$ W/m <sup>2</sup> .K <sup>4</sup> )
σ <sub>s</sub>	Scattering coefficient [1/m]
Φ	Phase function
φ	Porosity
Ω'	Solid angle [sr]
<i>Subscripts</i>	
c	Cold
cond	Conduction
f	Fluid
h	Hot
p	Pore
rad	Radiation
s	Solid
tot	Total

deployable multistable structures [18]. To study the thermo-fluidic characteristics in porous materials, four flow-regimes have been identified based on the pore diameter ( $d_p$ ) and Reynolds number ( $(Re_p = \frac{\rho V d_p}{\mu})$ ) of fluid that passes through the medium: (1) Darcy or creeping flow regime ( $Re_p < 1$ ), (2) Forchheimer flow regime ( $1 \sim 10 < Re_p < 150$ ), (3) Post-Forchheimer flow regime or unsteady laminar flow ( $150 < Re_p < 300$ ), and (4) Fully turbulent flow ( $Re_p > 300$ ) [19,20]. In addition to the porous materials with random pore architectures (*foams*), flow and heat transfer in periodic *lattice* materials with rationally-designed architectures have recently been studied and/or optimized theoretically, numerically, and experimentally, mainly due to the advances in additive manufacturing technologies and high-performance computing. A brief review on the thermo-fluidic characteristics of foams and lattices are laid out here.

One of the first attempts to study the pressure drop in porous materials was made by Darcy [21]. Porous materials cause resistance against the flow of fluid and imposes an extra pressure drop, which is considerable at lower porosities and higher Reynolds numbers. Lower pressure drop of foams and lattices has been considered as a major factor in the design and optimization of these porous media [22–24]. In this regard, other characteristics of fluid flow in foams and lattices, e.g. permeability and friction factor, have been extensively investigated [25–27]. Another important property of porous materials is their effective thermal conductivity with contributions from *convective thermal conductivity* between solid walls of porous materials and surrounding fluid, *radiative thermal conductivity* of solid walls, *solid thermal conductivity* of constitutive materials, and *fluid thermal conductivity* [28]. Convective thermal conductivity may be neglected when pore sizes are small and flow conditions are at ambient temperature and pressure [29,30]. In many studies when temperature is not high, the radiation mechanism has been also neglected when evaluating the effective thermal conductivity of porous materials. Therefore, most of the experimental [31,32], theoretical [33–35], or numerical [36–39]

investigations are centered around the conductive thermal conductivity, i.e. the combined effects of thermal conductivity of solid constituent and surrounding fluid of cellular solids [40]. Closed-form models have been developed to calculate the conductive thermal conductivity, covering a wide variety of foams and lattice architectures. These models calculate the conductive thermal conductivity as a function of solid and fluid thermal conductivity, porosity, and architectural parameters of cellular solids [33–35,41,42]. Numerous studies have explored the effect of forced convection in porous materials. For example, some studies have been performed on different types of heat exchangers (double pipe [43], shell and tube [44], and compact [45,46] heat exchangers) using foams and lattices to increase heat transfer rate and efficiency while trying to keep the pressure drop to a minimum level. Several correlations have also been proposed to calculate the Nusselt number in porous media, which are usually a function of porosity, Reynolds and Prandtl numbers, and geometrical parameters [47–49]. Enhancing the Nusselt number has also been achieved by introducing new lattice architectures, as an X-lattice cored rectangular based on honeycomb and X-lattice sandwich panel [50] and the plate fin-pyramidal lattice sandwich panel based on plate fin and pyramidal lattice sandwich panels [51]. Recent investigations have made strides to compare some thermo-fluidic characteristics of lattice materials with alternative architectures. For example; effective thermal conductivity, pressure drop, and Nusselt number of body centered cubic (BCC), face centered cubic (FCC), and A15 (similar to a Weaire-Phelan unit cell) lattices have been compared [52]; convective heat transfer and pressure drop in Kagome and tetrahedral truss lattices [53], Kagome and WBK sandwich panels [54], X-lattice and Pyramidal lattice sandwich panels [55], and Lord Kelvin and Weaire-Phelan lattices [56] have been explored; and the flow and end-wall heat transfer characteristics has been measured and compared for 3D printed lattice-frame structures of octahedron family [57] and FCC lattices made out of circular, rectangular, and elliptical cross-sections [58]. These studies have been led to selecting the best lattice architecture, based on forced convection heat transfer characteristics.

Radiation heat transfer becomes important when porous materials

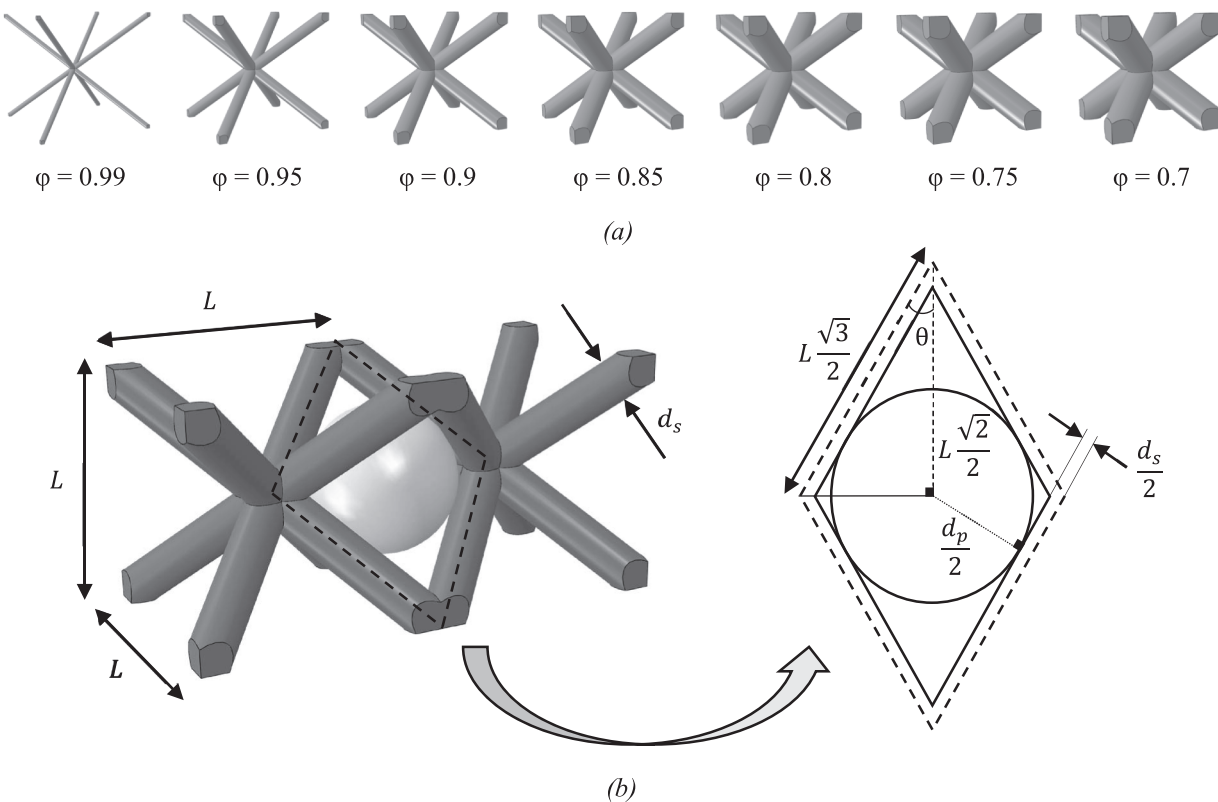


**Fig. 1.** (a) BCC lattice unit cell with alternative porosities and (b) Equivalent pore defined based on the neighboring unit cells.

are used in high-temperature applications such as solar receivers [59] or combustors [60]. Some authors considered the effect of radiation and obtained the radiative thermal conductivity for foams and lattices of cubic, dodecahedral, and tetrakaidecahedral architectures [61–63]. Among these studies, investigation has been done on the effects of porosity, pore density, and surface reflection on radiative properties of a few idealized lattices (Dul'nev, Viskanta, and cubic cells) [64]; thermal design and optimization of ceramic lattices with rotated cubic cells has been performed to maximize the radiative heat transfer for tubular high temperature heat exchanger applications [65]; positive volumetric effect and high solar-to-thermal efficiency have been obtained in the numerical study of convection and radiation heat transfer in solar receivers with honeycomb absorbers [66]; analysis has been done on the coupled radiation and forced convection heat transfer in a channel with constant temperature walls filled with periodic structure extracted from the tetrakaidecahedral model [67]; the coupled radiation and conduction heat transfer have been explored with the contact resistance boundary condition to study vacuum insulation panels using porous materials [68]; the share of radiation in the total heat transfer has been obtained in the simulation of conduction, convection, and radiation heat transfer in a solar receiver filled with open cell foams [59]; and a multiscale asymptotic expansion method has been developed for predicting three modes of heat transfer in periodic lattice architecture (a combination of pipes and cavities) [69].

Due to recent advances in 3D printing technology and the possibility of fabricating multifunctional materials with complex nano/micro-architectures, rationally-designed lattices constituting metamaterials and *meta*-structures have received much attention [70–74]. In addition to their mechanical properties [75–78], the hydrodynamic and thermal behavior of architected lattices when considering different heat transfer modes under alternative boundary conditions is of great importance. Since developing an accurate analytical model for combined convective-radiative heat transfer problems is unfeasible, a computational study based on the finite volume method (FVM) or finite element method

(FEM) is essential. Among alternative lattice architectures, much research has been conducted on the mechanical properties of BCC lattices, as an example of cubic cellular architectures, owing to their facile fabrication process using additive manufacturing or molding and their engineering applications as energy engineering, construction, transportation, aerospace, etc. [79–84]. However, to the best of the authors' knowledge, a comprehensive study that includes contributions of all three modes of heat transfer for the BCC lattices under alternative boundary conditions has not yet been conducted. It is also critical to compare the thermal behavior of lattices in the absence and presence of radiation since this mechanism is commonly ignored to simplify the evaluation of thermal performance of architected lattices. The present study ascertains situations where radiation heat transfer cannot be overlooked in the thermal analysis of BCC lattices, by comparing the results in the absence and the presence of radiation heat transfer. The current study focuses on BCC lattices as a representative of cubic cellular architectures, among a plethora of cell architecture, to better understand different modes of heat transfer in lattice materials for a wide range of porosity, rather than investigating the effect of cell topology on the heat transfer process. Similar analyses can also be performed for alternative cellular lattices with arbitrary architectures based on the methodology presented in this study.

In this paper, the architecture of BCC lattices is first introduced in Section 2.1. Equations for calculating the equivalent pore diameter and specific surface area are derived. The governing equations, boundary conditions, mesh description, and verification are presented in Sections 2.2 to 2.4. The hydrodynamic behavior of the BCC lattices is studied in Section 3. In the present study, conduction and convection heat transfers in BCC lattices are explored using two types of thermal conditions: (1) Constant temperature at solid struts and (2) Constant heat release from the solid struts. Finally, radiation heat transfer is added to the heat transfer modes, and its effects on the overall heat transfer and effective thermal conductivity is elicited.

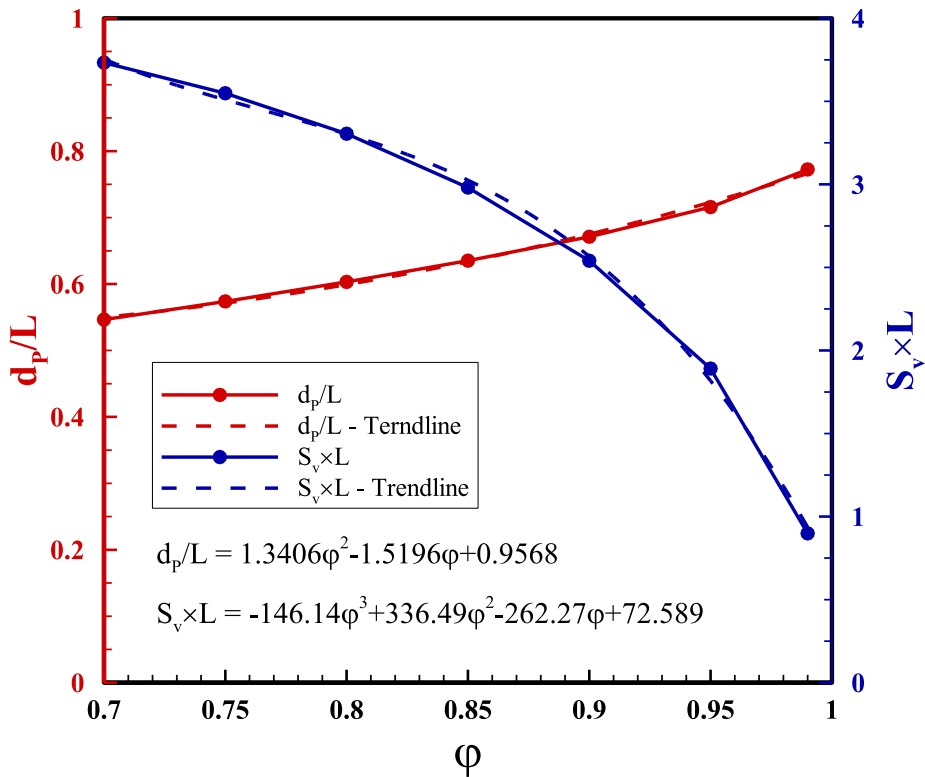


Fig. 2. Normalized equivalent pore diameter and normalized specific surface area as a function of lattice porosity.

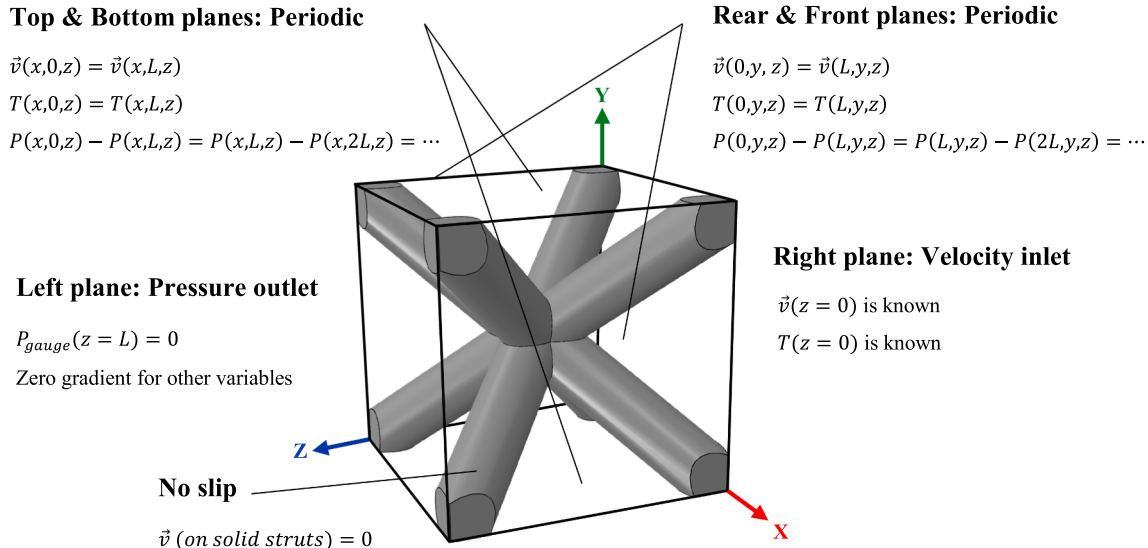


Fig. 3. Boundary conditions for the BCC lattice unit cell.

## 2. Numerical simulation

### 2.1. Geometry of the unit cell

In this paper, the architecture of the three-dimensional unit cell is inspired from BCC crystals in the cubic family of crystal systems, produced by SolidWorks software and numerically analyzed via the Fluent software (Fig. 1a). As the cell size remains unchanged, the porosity of cell varies by tailoring the diameter of cylindrical struts in the BCC unit cell. Porosity is defined as the ratio of the empty volume in the unit cell to the total cell volume. The equivalent pore diameter is defined as the diameter of the largest sphere encapsulated by the struts of unit cell

[85]. If two neighboring cubic cells are considered (Fig. 1b), the equivalent pore diameter is calculated by:

$$\frac{d_p}{2} = \frac{L\sqrt{2}}{2} \sin\theta - \frac{d_s}{2} \quad (1)$$

where  $\theta = \cos^{-1}\frac{L\sqrt{2}/2}{L\sqrt{3}/2} = 35.264^\circ$  and  $d_s$  presents the strut diameter of the BCC lattice. For the unit cells with  $a \times b \times c$  dimension, the pore diameter can be calculated similarly as presented in appendix A. One of the other desired characteristics of porous media is their high specific surface area ( $S_v$ ), defined as the area of solid struts to the total volume of unit cell. The equivalent pore diameter and the specific surface area,

**Table 1**  
Thermophysical properties of the fluid and constituent solid.

Material	Thermal conductivity (W/m. K)	Density (kg/m <sup>3</sup> )	Specific heat (J/kg.K)	Viscosity (kg/m.s)
Fluid	0.0265	from EOS	1006.43	$1.7894 \times 10^{-5}$
Solid	218	2719	871	–

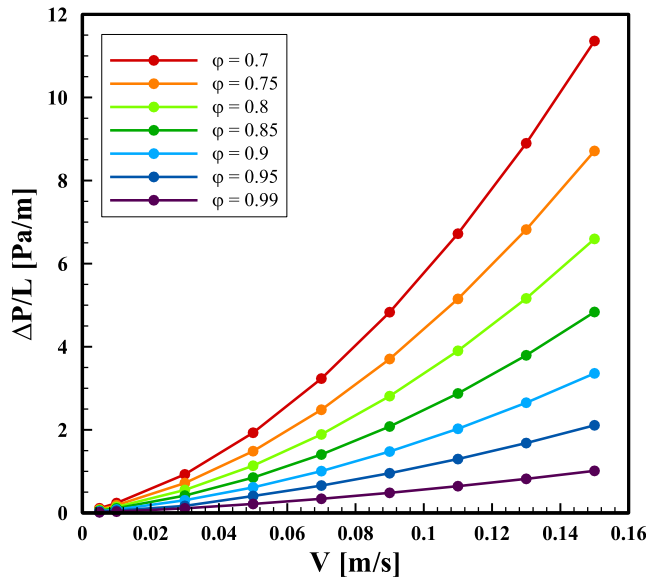


**Fig. 4.** Pressure drop per unit cell size as a function of the superficial velocity for alternative porosities of BCC lattices.

normalized by the BCC lattice cell size, is presented in Fig. 2. Quadratic and cubic polynomial equations have been used to interpolate the results for the normalized equivalent pore diameter and specific surface area.

## 2.2. Governing equations

In this section, the governing equations for the simulation of fluid flow and heat transfer in porous media are presented. These equations are simplified based on steady-state, incompressible flow, and temperature-independent material property assumptions. The corresponding continuity, momentum, and energy conservation equations along with the Discrete Ordinates equation for radiation heat transfer are presented as [86,87]:

$$\nabla \cdot (\rho \vec{v}) = 0 \quad (2a)$$

$$\rho (\vec{v} \cdot \nabla \vec{v}) = -\nabla P + \mu \nabla^2 \vec{v} \quad (2b)$$

$$\rho C_p (\vec{v} \cdot \nabla T) = \nabla \cdot (k \nabla T) + \dot{q} \quad (2c)$$

$$\begin{aligned} \nabla \cdot (I(\vec{r}, \vec{s}) \vec{s}) + (a + \sigma_s) I(\vec{r}, \vec{s}) &= an^2 \frac{\sigma T^4}{\pi} \\ &+ \frac{\sigma_s}{4\pi} \int_0^{4\pi} I(\vec{r}, \vec{s}') \Phi(\vec{s}, \vec{s}') d\Omega' \end{aligned} \quad (2d)$$

where  $\vec{v}$  is velocity vector,  $\rho$  is density,  $P$  is pressure,  $\mu$  is dynamic viscosity,  $C_p$  is specific heat,  $T$  is temperature,  $k$  is thermal conductivity,  $\dot{q}$  is the heat generation,  $I$  is radiation intensity,  $\vec{r}$  is position vector,  $\vec{s}$  is direction vector,  $\vec{s}'$  is scattering direction vector,  $a$  is absorption coefficient,  $\sigma_s$  is scattering coefficient,  $n$  is reflective index,  $\sigma$  is the Stefan-

Boltzmann constant,  $\Phi$  is the phase function, and  $\Omega'$  represents solid angle. All mentioned equations are used for fluid phase, and Eq. (2c) is used for both fluid and solid phases. For solid phase, the left side of Eq. (2c) is zero.

## 2.3. Boundary conditions and mesh description

Boundary conditions for the unit cell with 1.5 cm size are shown in Fig. 3. The flow direction is in z-direction. Therefore, the velocity inlet boundary condition is used for the right plane (the inlet plane), where cool air enters at a temperature of 300 K with a velocity corresponding to the specified Reynolds number. Pressure outlet boundary condition is used for the left plane (the outlet plane), and the no-slip boundary condition is used for the internal walls (struts) between solid and fluid inside the domain. For the other boundaries on four sides of the cube (top and bottom planes perpendicular to the y-coordinate, and rear and front planes perpendicular to the x-coordinate), the periodic boundary condition is used. Two types of thermal conditions, namely a constant temperature of 700 K at solid strut surfaces and a constant heat release of 2 W from the solid struts, have been considered for the numerical simulations. These types of boundary conditions are adopted to assess the performance of the lattice materials and structures under quite different conditions. Therefore, the assigned values that are used in the aforementioned boundary conditions are arbitrary.

The ANSYS meshing tool is used to generate computational unstructured meshes for the simulations. To ensure that the results are independent of the grid, different element numbers are examined. The results show that about  $2 \times 10^5$  elements are appropriate for a grid-independent solution on a unit cell. The structure of the mesh for the unit cell at different cross-sections is shown in Appendix B. Table 1 presents the thermophysical properties of the solid struts and the air passing through the BCC lattice. It is also assumed that the melting temperature of the constituting solid is beyond the temperature range considered in this paper.

## 2.4. Verification

Verification study of the adopted approach is performed in two parts. A combined conduction-convection heat transfer problem, like the one presented in [36], is considered, and then a radiation heat transfer problem [88,89] is studied. Both cases are presented in Appendix C where a good agreement is achieved between the simulated and the existing published results.

## 3. Results and discussion

### 3.1. Pressure drop and permeability

Recalling the definition of flow regime and considering Reynolds numbers in the Forchheimer region ( $Re_P = 1-150$ ), the pressure drop equation in the unit cell may be written as:

$$-\frac{dP}{dz} = \frac{\mu}{\kappa} V + \frac{\rho C_f}{\sqrt{\kappa}} V^2 \quad (3)$$

where  $\frac{dP}{dz}$ ,  $V$ ,  $\kappa$ , and  $C_f$  are, respectively, pressure gradient along the main direction of flow, superficial velocity, permeability, and inertia coefficient;  $\alpha = \frac{\mu}{\kappa}$  and  $\beta = \frac{\rho C_f}{\sqrt{\kappa}}$  can also be defined as Darcy and non-Darcy coefficients. Fig. 4 shows the pressure drop between the inlet and the outlet planes, per unit cell size at different superficial velocities. As the superficial velocity increases, the pressure drop increases; the variation is linear at lower superficial velocities (Darcy region) and is nonlinear at higher superficial velocities (non-Darcy region). The pressure drop also enhances by the porosity reduction of the lattice, because of the increase of resistance caused by solid struts to flow for lattices with lower

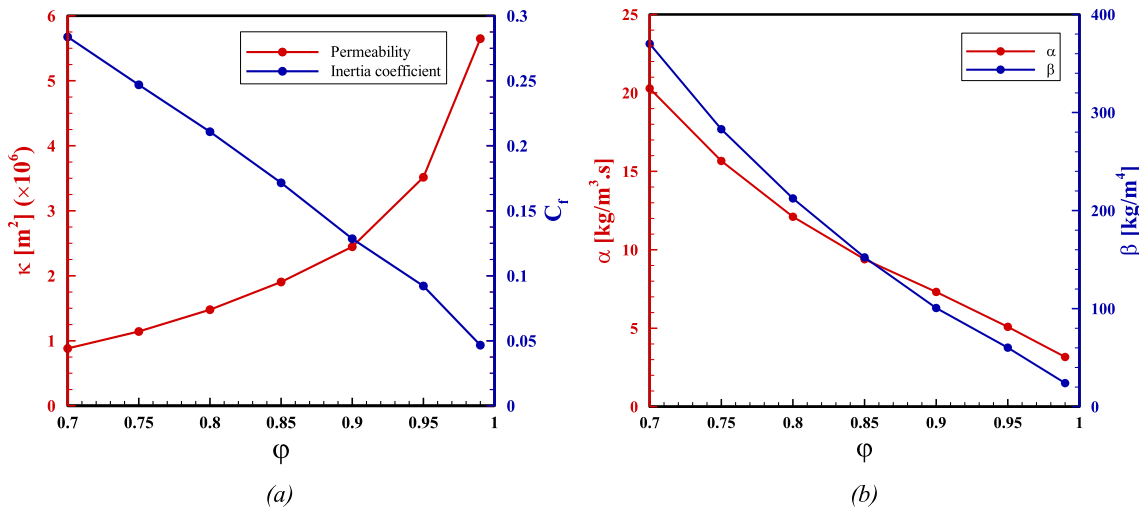


Fig. 5. (a) Permeability and inertia coefficient and (b) Darcy and non-Darcy coefficients as a function of lattice porosity.

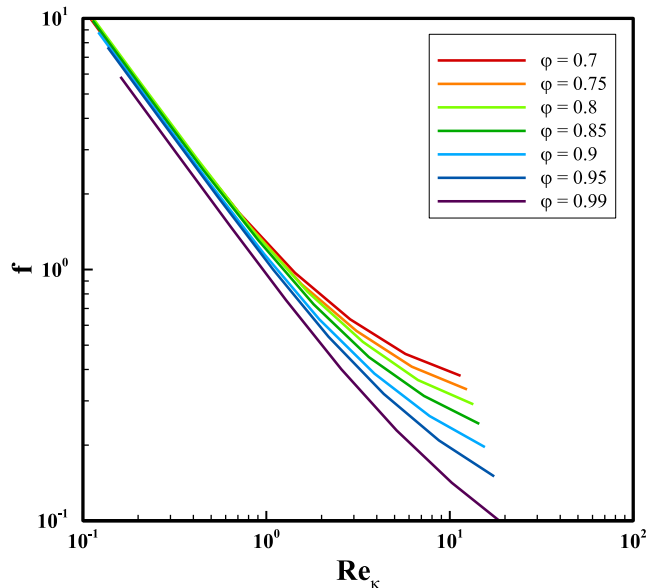


Fig. 6. Friction factor for different porosities of BCC lattices as a function of Reynolds number.

porosities. By fitting a quadratic equation to data in Fig. 4, the permeability, inertia coefficient, and Darcy and non-Darcy coefficients are calculated by Eq. (3) and are presented in Fig. 5. As the overall cell shape remains unchanged in the form of BCC lattices, permeability varies only by porosity in this study. Due to the inverse relationship of permeability and pressure drop, permeability decreases when porosity decreases. In opposite, the other three coefficients (i.e. inertia coefficient, and Darcy and non-Darcy coefficients) are directly related to pressure drop and increase when porosity decreases.

### 3.2. Friction factor

Exploiting the calculated pressure drop and permeability in previous section, the friction factor ( $f$ ) in the BCC lattice unit cell is determined by the following equation and presented in Fig. 6 as a function of Reynolds number based on the permeability ( $Re_\kappa = \frac{\rho V \sqrt{\kappa}}{\mu}$ ):

$$f = \frac{-\frac{dp}{dz} \sqrt{\kappa}}{\rho V^2} = \frac{1}{Re_\kappa} + C_f \quad (4)$$

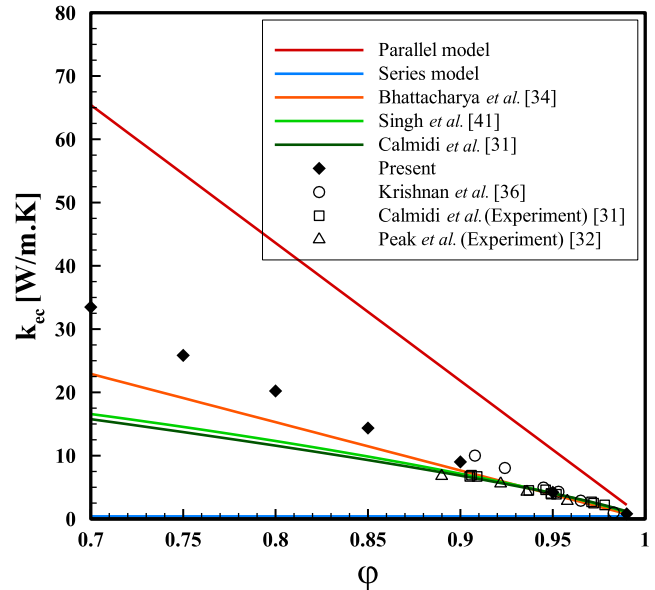
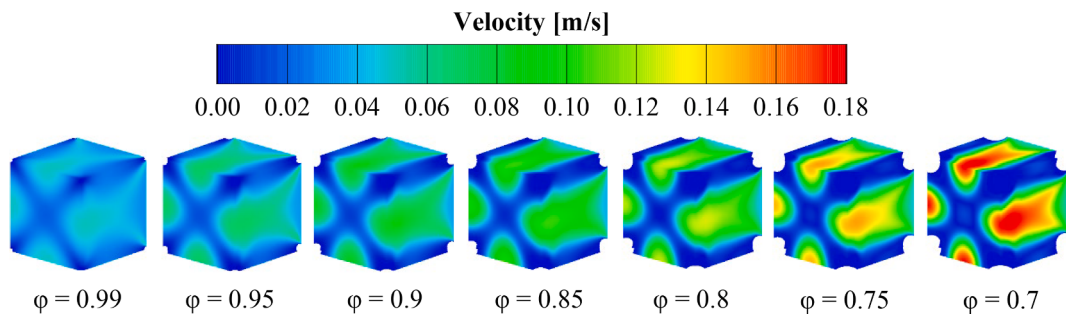


Fig. 7. Conductive thermal conductivity as a function of lattice porosity.

When the porosity of the unit cell decreases at a constant Reynolds number, the permeability decreases, opposed to the pressure drop and superficial velocity. The pressure drop has a more significant effect on friction factor; as a result, the friction factor increases as the porosity decreases (Fig. 6). Furthermore, at a constant porosity, the friction factor decreases by increasing the Reynolds number and velocity. The associate inertia coefficient in the right side of the Eq. (4), shown in Fig. 5a, was also calculated in the literature for other porous media geometries [32,90,91].

### 3.3. Conductive thermal conductivity

In this section, by ignoring the thermal radiation effect, a certain temperature gradient is applied to the two opposite faces on the left and right of the BCC lattice unit cell (Fig. 3), (in both solid and fluid phases). The other sides of the unit cell are kept under adiabatic conditions. In this case,  $Re = 0$  since the fluid is in a stagnant state and coupled boundary condition is applied for the internal walls (struts). By calculating the heat flux between the two opposite faces (in both solid and fluid phases), conductive thermal conductivity ( $k_{ec}$ ), representing the



**Fig. 8.** Velocity contours for alternative porosities for BCC lattices with  $Re_p = 25$  for constant temperature boundary condition.

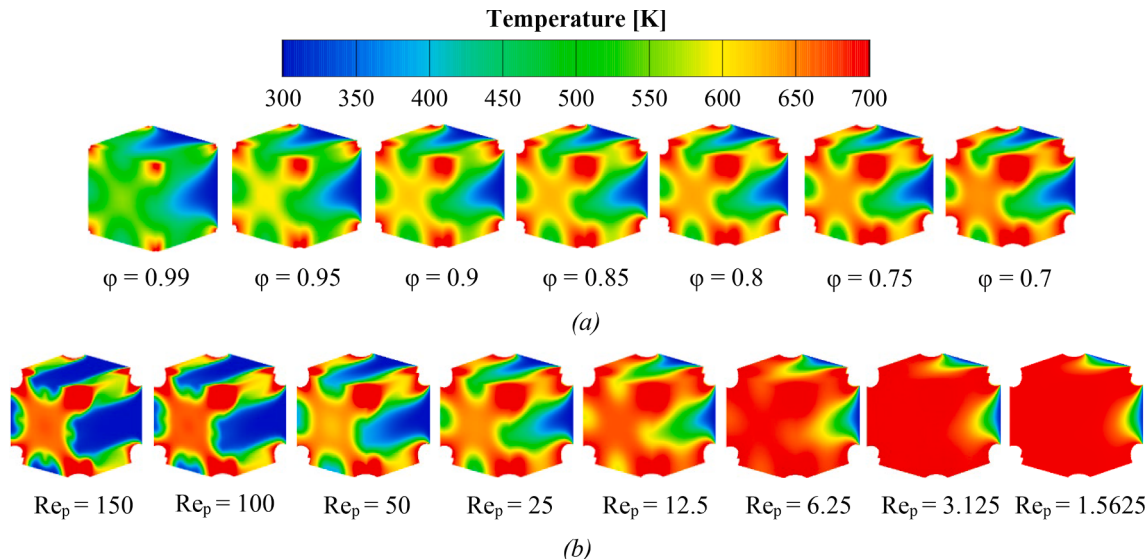


**Fig. 9.** Temperature contours of fluid for (a) alternative porosities with  $Re_p = 25$  and (b) alternative Reynolds numbers with  $\varphi = 0.7$  for BCC lattices and constant temperature boundary condition.

combined effects of solid and fluid thermal conductivity, is calculated by:

$$k_{ec} = \frac{-\int q.dA}{\frac{\partial T}{\partial z} A} = \frac{-\left( \int_s q.dA_s + \int_f q.dA_f \right)}{\frac{\partial T}{\partial z} (A_s + A_f)} \quad (5)$$

where  $q$  is the heat flux,  $A$  is the cross-section area,  $\frac{\partial T}{\partial z}$  is the temperature gradient, and  $s$  and  $f$  represent, respectively, the solid and fluid phases. Fig. 7 shows that the conductive thermal conductivity increases when porosity decreases (the amount of the solid phase in the unit cell increases) due to the higher contribution of solid thermal conductivity compared to that of fluid. It can be seen that the parallel and series models specify the upper and lower bounds. Moreover, the calculated conductive thermal conductivity is in good agreement with the available results for  $\varphi > 0.9$ . Numerical results also show that the conductive thermal conductivity does not change with the applied temperature difference or the cell size of lattices. Due to the cubic anisotropy of the BCC lattices considered in this study, it is worth mentioning that the normal conductive thermal conductivity is the same in all three directions.

### 3.4. Constant temperature boundary condition

After applying a constant temperature boundary condition of 700 K to the solid struts, the heat transfer and fluid flow in the BCC lattices with alternative porosities are investigated in this section for various Reynolds numbers based on the pore diameter ( $Re_p$ ).

#### 3.4.1. Velocity field

Fig. 8 presents the velocity field inside the BCC lattices with alternative porosities at  $Re_p = 25$ . As the porosity decreases at a constant Reynolds number, the equivalent pore diameter in the cell decreases, so the inlet fluid velocity increases. On the other hand, as the porosity decreases and the solid struts become more extensive, the cross-sectional area for flow decreases, so the velocity in the cell increases again. Obviously, at a constant porosity, the velocity in the cell increases with increasing the Reynolds number. Moreover, due to the no-slip boundary condition on the solid struts, the velocity near these areas is zero.

#### 3.4.2. Temperature field

Fig. 9a shows the temperature field inside the geometries with alternative porosities at  $Re_p = 25$ . As the Reynolds number remains constant and the porosity decreases, two opposing events take place. First, the solid surface area increases, which is expected to warm the cell, as the solid temperature is 700 K. Second, the fluid local velocity increases, which is expected to cool the cell as the fluid inlet temperature is 300 K. However, the former process is dominant, so as the porosity decreases, the cell temperature increases. The temperature in the cell is also higher near solid struts. Fig. 9b shows the effect of changing the Reynolds number on a constant porosity of 0.7. Results show that cell temperature is decreased by increasing the Reynolds number and the flow ability to cool the cell. Clip. 1 shows the temperature changes inside the cells presented in Fig. 9b, and Clip. 2 shows these temperature changes from another view for  $\varphi = 0.7$  and  $Re_p = 150$ , which shows the more pronounced temperature changes.

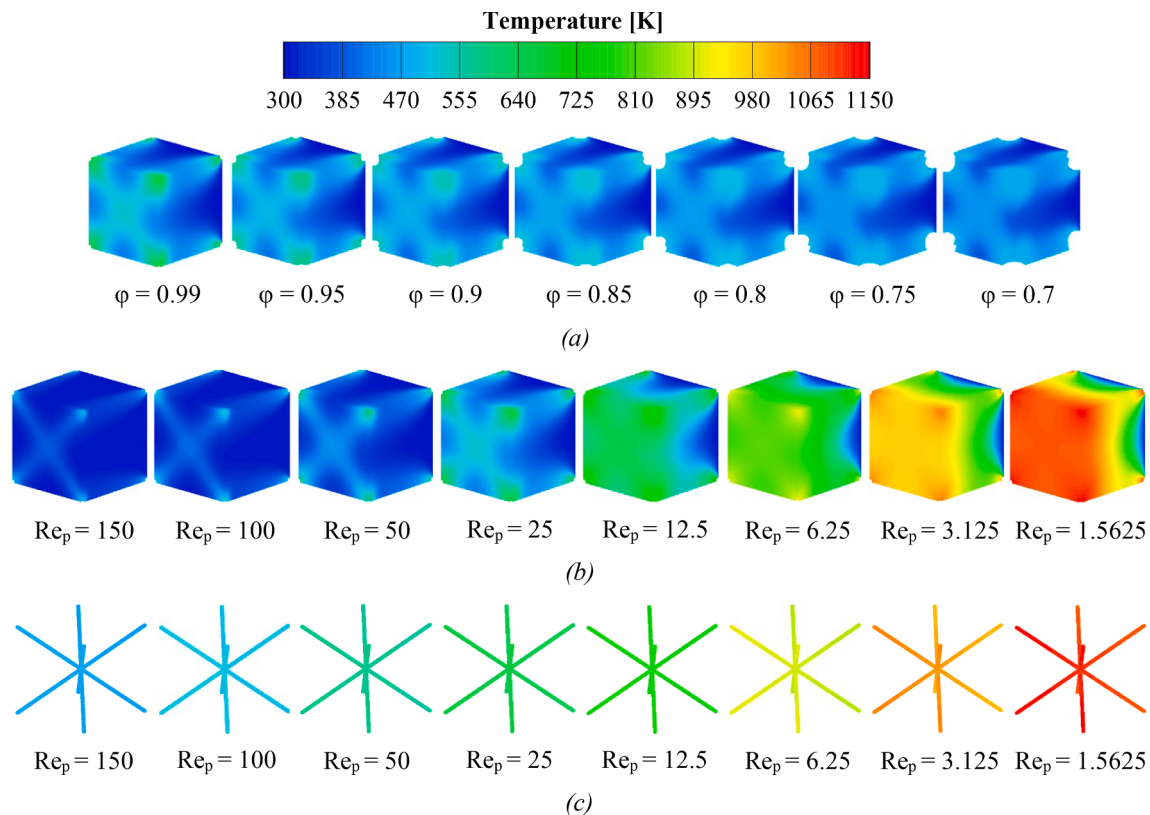


**Fig. 10.** Temperature contours of fluid for (a) alternative porosities with  $Re_p = 25$ , (b) alternative Reynolds numbers with  $\varphi = 0.99$ , and (c) temperature contours of solid struts for alternative Reynolds numbers with  $\varphi = 0.99$  for BCC lattices and constant heat release thermal condition.

### 3.5. Constant heat release thermal condition

After applying a constant amount of 2 W heat rate to the solid struts, the fluid flow and heat transfer with different Reynolds numbers in the geometries with alternative porosities are investigated. The velocity field is similar to the previous boundary condition.

#### 3.5.1. Temperature field

Fig. 10a shows the temperature field inside the geometries with different porosities at  $Re_p = 25$ . Due to the type of thermal condition applied, the temperature change trend is the opposite of the previous case. Applying a constant amount of 2 W heat rate in the geometries with different porosities causes the solid struts in the samples with higher porosities to heat up more and make the fluid around themselves warmer. On the other hand, as mentioned before, with increasing the porosity, the fluid velocity and its ability to reduce the cell temperature decreases. Together, these two factors cause the cell temperature to increase as the porosity increases. Fig. 10b and Fig. 10c show the fluid and solid struts temperature at a constant porosity of 0.99, respectively. It can be seen that the inlet velocity increases as the Reynolds number increases, so the temperature of the fluid and solid struts decrease. Temperature changes at different cross-sections of the unit cell and variation of solid struts temperature along the flow direction are also shown in Appendix C. Clip. 3 shows the temperature changes inside the cells presented in Fig. 10b, and Clip. 4 shows these temperature changes from another view for the  $\varphi = 0.99$  and  $Re_p = 1.5625$ , which has the most temperature changes.

### 3.6. Radiation effects

In this section, the addition of thermal radiation mechanism on the heat transfer in BCC lattices is studied. First, its influence on the effective thermal conductivity is investigated. Then, for the constant heat release

thermal condition, fluid flow and conduction, convection, and radiation heat transfer are simulated. The Discrete Ordinates Method is used for the simulation of radiation heat transfer in the Fluent software [87].

#### 3.6.1. Radiative thermal conductivity

Similar to Section 3.3; first, a thermal gradient of 200 K is applied to a pair of opposing faces of the unit cell, then radiative thermal conductivity ( $k_{er}$ ) and effective thermal conductivity ( $k_{eff}$ ) are calculated by:

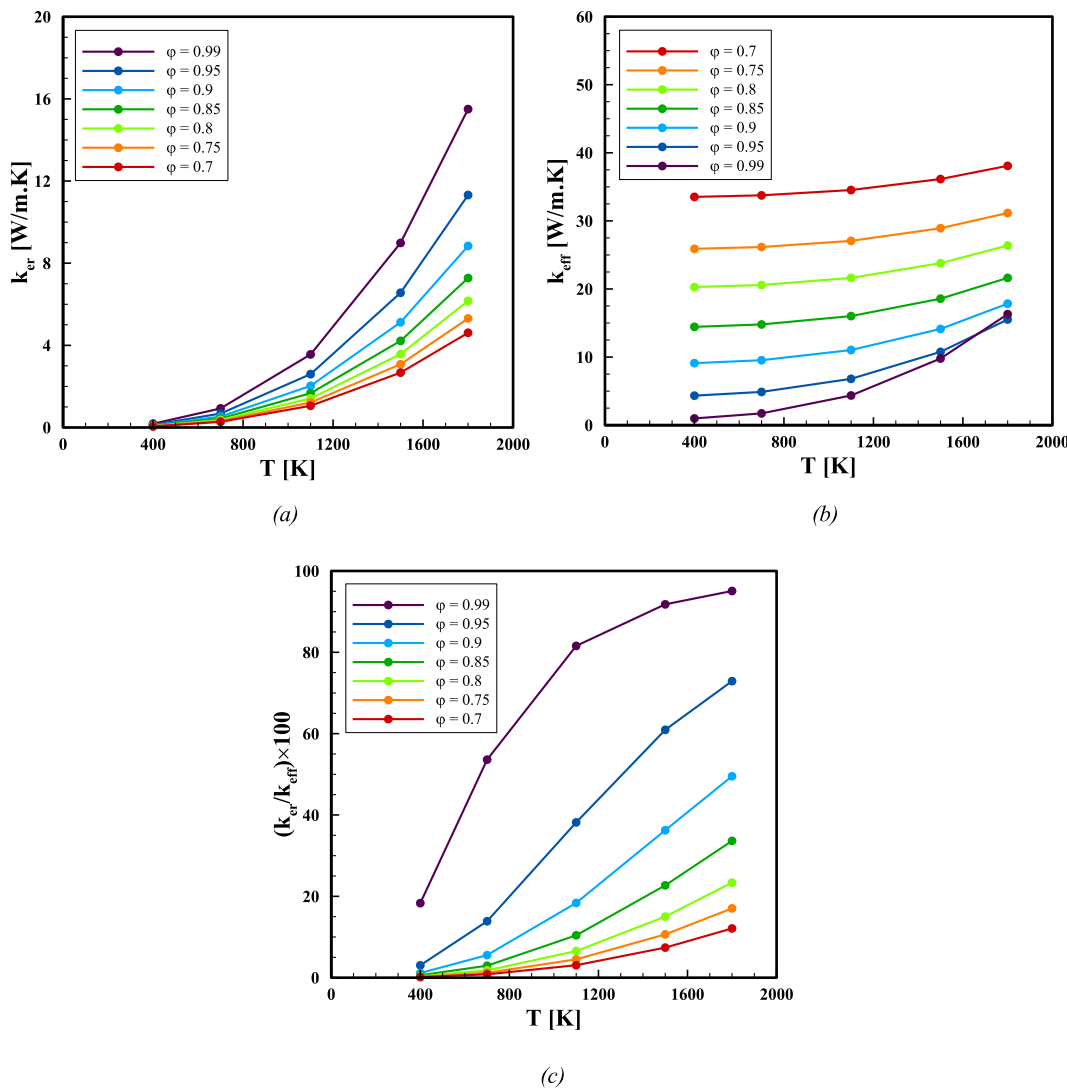
$$q = q_{cond} + q_{rad} = -(k_{ec} + k_{er}) \frac{\partial T}{\partial z} = -k_{eff} \frac{\partial T}{\partial z} \quad (6)$$

Fig. 11 shows profiles of radiative thermal conductivity, effective thermal conductivity, and radiation contribution of effective thermal conductivity as a function of mean temperature ( $T = \frac{(T_h + T_c)}{2}$ , where  $T_h$  and  $T_c$  are the temperatures applied to opposing faces of the unit cell) for different porosities. The solid emission coefficient is assumed to be 0.2, and for all surfaces, diffuse and gray radiation conditions are presumed. As shown in Fig. 11a,  $k_{er}$  monotonically increases versus mean temperature, with a more steep slope at higher mean cell temperatures, because radiation is more significant at higher temperatures. By curve-fitting the simulation results, a cubic polynomial, Eq. (7a), fits the variation of  $k_{er}$  in terms of mean temperature. The coefficients of Eq. (7a) in terms of porosity, are presented by the following equations.

$$k_{er} = C_0 + C_1 T + C_2 T^2 + C_3 T^3 \quad (7a)$$

$$C_0 = 3.2541 \times 10^{-1} \varphi^3 - 7.9657 \times 10^{-1} \varphi^2 + 6.5487 \times 10^{-1} \varphi - 1.7919 \times 10^{-1} \quad (7b)$$

$$C_1 = 4.2060 \times 10^{-4} \varphi^3 - 1.0209 \times 10^{-3} \varphi^2 + 8.3162 \times 10^{-4} \varphi - 2.2354 \times 10^{-4} \quad (7c)$$



**Fig. 11.** (a) Radiative thermal conductivity, (b) Effective thermal conductivity, and (c) Radiation contribution of effective thermal conductivity of BCC lattices as a function of mean temperature for alternative porosities.

$$C_2 = 1.2433 \times 10^{-6} \varphi^3 - 2.8638 \times 10^{-6} \varphi^2 + 2.2182 \times 10^{-6} \varphi - 5.6930 \times 10^{-7} \quad (7d)$$

$$C_3 = 1.2253 \times 10^{-7} \varphi^3 - 2.8659 \times 10^{-7} \varphi^2 + 2.2565 \times 10^{-7} \varphi - 5.8780 \times 10^{-8} \quad (7e)$$

In Section 3.3, it was observed that \$k\_{ec}\$ increases with decreasing the porosity, but as shown in Fig. 11a, \$k\_{er}\$ decreases by reducing the porosity at a constant mean temperature. The reason is due to the higher specific surface when porosity is reduced. Consequently, the radiated beams would be trapped within shorter paths, thus radiation energy is dissipated sooner, resulting in smaller radiation zone of influence and lower values for \$k\_{er}\$. Fig. 11b shows \$k\_{eff}\$, which is defined as the sum of \$k\_{ec}\$ and \$k\_{er}\$. It is observed that increasing the temperature at higher porosities causes a more significant increase in \$k\_{eff}\$, but in general, \$k\_{eff}\$ has higher values for lower porosities. In other words, at lower porosities, the conduction heat transfer, and at higher porosities, the radiation heat transfer play a dominant role in \$k\_{eff}\$. A noteworthy point in Fig. 11b is that at very high temperatures and high porosities (for example, at \$\varphi = 0.99\$), the value of \$k\_{er}\$ and consequently \$k\_{eff}\$ become so large that this \$k\_{eff}\$

is greater than the value of the corresponding \$k\_{eff}\$ at the same mean temperature but for a lower porosity (for example, at \$\varphi = 0.95\$). Fig. 11c shows the percentage of \$k\_{er}\$ from the \$k\_{eff}\$ at different mean cell temperatures and different porosities. As expected, based on the analysis of the previous graphs, at higher porosities and temperatures, \$k\_{er}\$ has a more influencing contribution in the \$k\_{eff}\$ (at the average cell temperature of 1800 K, the ratio of \$k\_{er}/k\_{eff}\$, is calculated 95% for the \$\varphi = 0.99\$, and is 12% for the \$\varphi = 0.7\$). Another point in this figure is the slope of the graphs, which shows that at a constant porosity, the profiles slope first increases with increasing temperature, but then it begins to decrease. At higher porosities, the increase in the slope is more obvious initially, but the temperature at which the slope begins to reduce is lower. To evaluate the effect of solid thermal conductivity, another solid material with thermal conductivity of 16.27 W/m.K is also used. Fig. 12 shows \$k\_{eff}\$ for this new material compared to Fig. 11b. In the new material, by reducing the solid thermal conductivity, and consequently the value of \$k\_{ec}\$, radiation contributes more in the \$k\_{eff}\$ values. \$k\_{eff}\$ is lower for the high porosities at low average temperatures, but by increasing the mean temperature, it becomes greater in high porosities than in low porosities.

### 3.6.2. Emissivity, temperature difference, and cell size effects on radiative thermal conductivity

As mentioned earlier, the solid radiative emission coefficient is

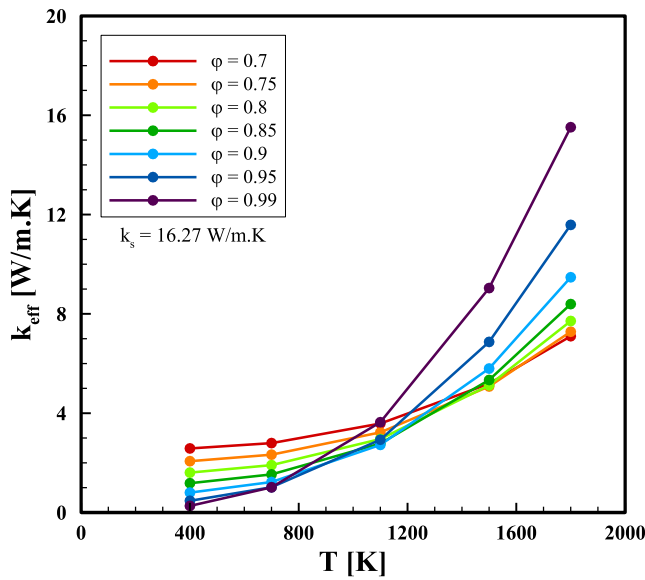


Fig. 12. Effective thermal conductivity of BCC lattices as a function of mean temperature for a solid material with  $k_s = 16.27$  W/m.K.

assumed to be 0.2. For the sample with  $\varphi = 0.99$  and  $T = 1800$  K, with the highest value of  $k_{er}$ , the changes of  $k_{er}$  are plotted versus the solid radiative emission coefficient in Fig. 13a. It is observed that for this sample,  $k_{er}$  can be increased by 12.5% when solid radiative emission coefficient increases from 0.05 to 1. Fig. 13a also shows the changes in  $k_{er}$  due to the amount of exerted temperature difference. By increasing the temperature difference, while the average cell temperature remains constant, the value of  $k_{er}$  rises slightly. For the temperature difference of 400 K compared to 2 K,  $k_{er}$  increases by 1.2%. Fig. 13b shows the changes in  $k_{er}$  as a cell size function. It is observed that as the cell size increases,  $k_{er}$  increases linearly. By increasing the cell size, the solid struts become proportionally larger to keep the porosity constant. Therefore, the radiation is emitted and reflected in a larger space, resulting in an increase in the radiation penetration thickness. This behavior causes a reduction of the thermal resistance, so the radiative thermal conductivity increases [61].

### 3.6.3. Combined conduction, convection, and radiation heat transfer

Similar to Section 3.5, fluid flow and heat transfer are simulated for the constant heat release thermal condition, this time in the presence of radiation. When radiation is not modeled, all of the applied heat is transferred by conduction and convection. By adding the radiation mechanism, the contribution of conduction and convection heat transfer decreases in favor of the contribution of radiation heat transfer. Fig. 14 shows that by reducing the Reynolds number and consequently increasing the solid struts temperature, the fraction of radiation heat transfer to the total heat transfer increases (for the  $\varphi = 0.99$ , this ratio increases six times as the Reynolds number decreases from 150 to 1.5625). Moreover, with decreasing the porosity and consequently the solid struts temperature, the contribution of radiation heat transfer decreases, but this reduction is marginal. Temperature contours are shown in Fig. 15 for a sample case with  $\varphi = 0.99$  and different Reynolds numbers with and without thermal radiation. It can be seen that by adding the radiation effect, while other conditions are similar, the cell temperature decreases.

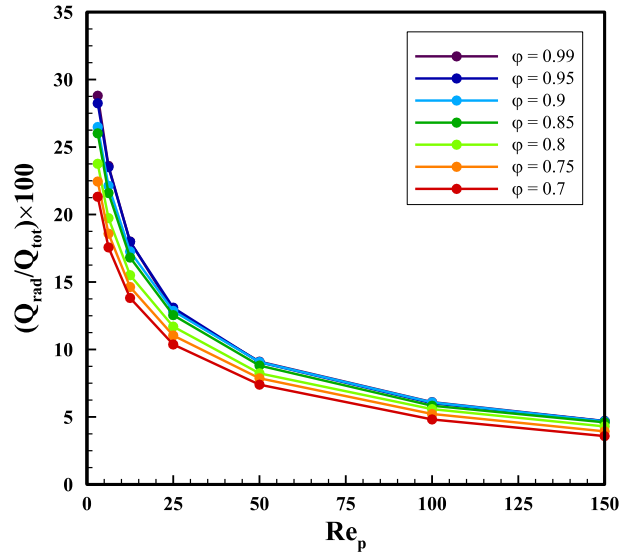


Fig. 14. The ratio of radiation heat transfer to the total heat transfer as a function of Reynolds number for BCC lattices.

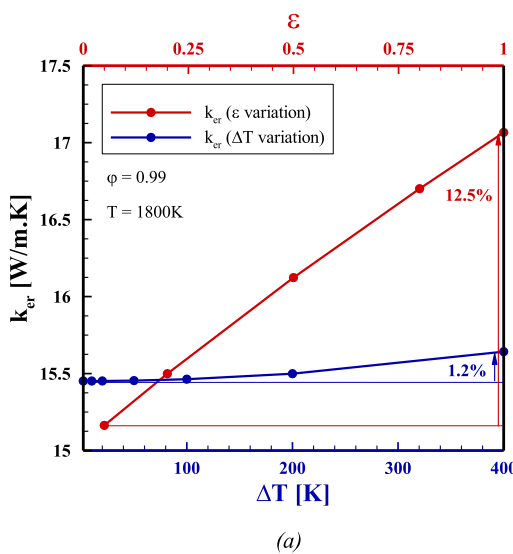
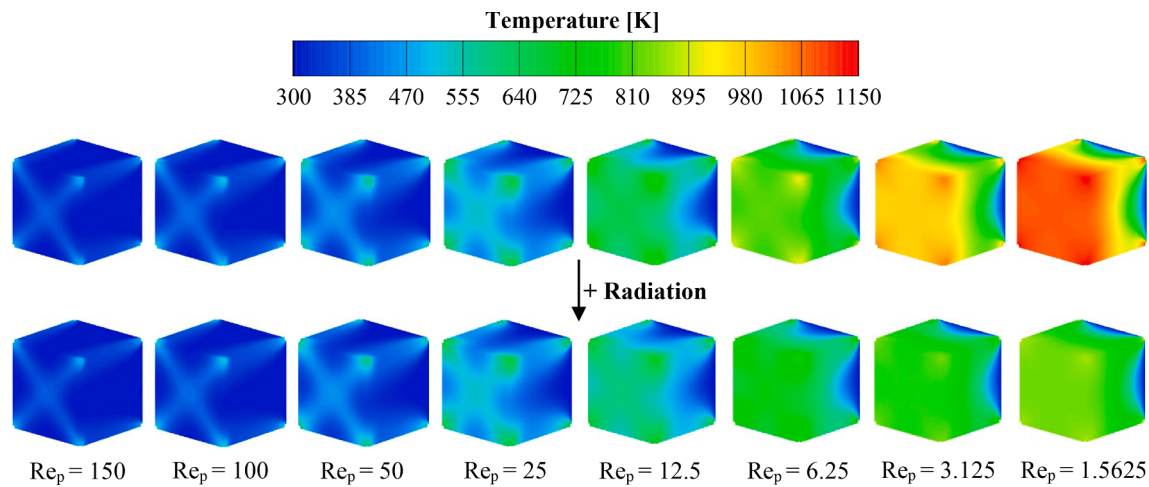
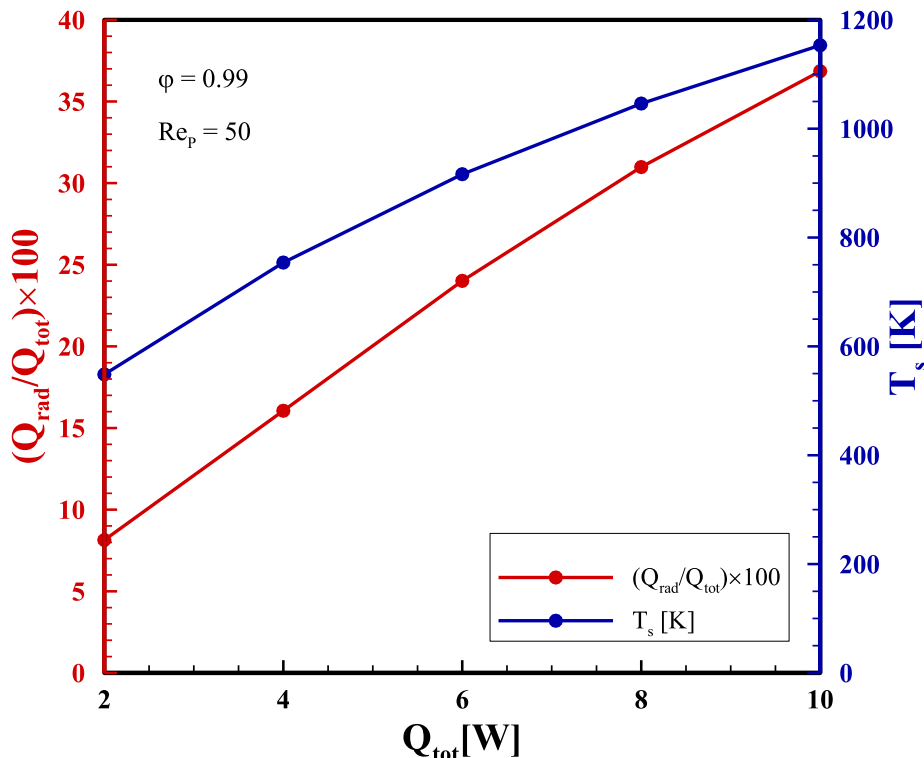


Fig. 13. The effects of (a) solid emission coefficient and applied temperature difference, and (b) cell size on the radiative thermal conductivity of BCC lattices with  $\varphi = 0.99$  and mean temperature of 1800 K.



**Fig. 15.** Temperature contours of fluid in the absence and presence of radiation heat transfer for different Reynolds numbers for BCC lattices with  $\varphi = 0.99$  and constant heat release thermal condition.



**Fig. 16.** The ratio of radiation heat transfer to the total heat transfer, and mean solid struts temperature as a function of the amount of heat release for BCC lattices with  $\varphi = 0.99$  and  $Re_p = 50$ .

#### 3.6.4. Effect of constant heat release thermal condition on the radiation heat transfer

In this section, for the sample case with  $\varphi = 0.99$  and  $Re_p = 50$ , the effect of the amount of heat transferred by the solid is investigated. Fig. 16 shows that as the amount of heat released in the solid struts increases, the solid struts temperature rises, so the ratio of radiation heat transfer to the total heat transfer increases.

#### 4. Concluding remarks

In this paper, fluid flow and conduction, convection, and radiation heat transfer in open-cell BCC lattices with porosities in the range of 0.7 to 0.99 have been numerically studied under two different thermal

conditions, i.e., *Constant temperature at solid struts* and *Constant heat release from the solid struts*. Due to the non-spherical pores in the BCC lattices, a relationship is presented to calculate the equivalent pore diameter. While the mechanical properties of this cellular architecture have been extensively studied, a comprehensive study on different heat transfer modes in this cell is yet to be reported to facilitate the application of engineered multifunctional cellular metamaterials in lightweight and load-bearable structures with heat exchanging functionalities. Initially, the hydrodynamic characteristics of the flow in the unit cells are explored. Opposed to permeability, it is demonstrated that pressure drop, inertia coefficient, Darcy and non-Darcy coefficients, and friction factor increase by decreasing the porosity. The conductive thermal conductivity is then calculated, which increases by decreasing

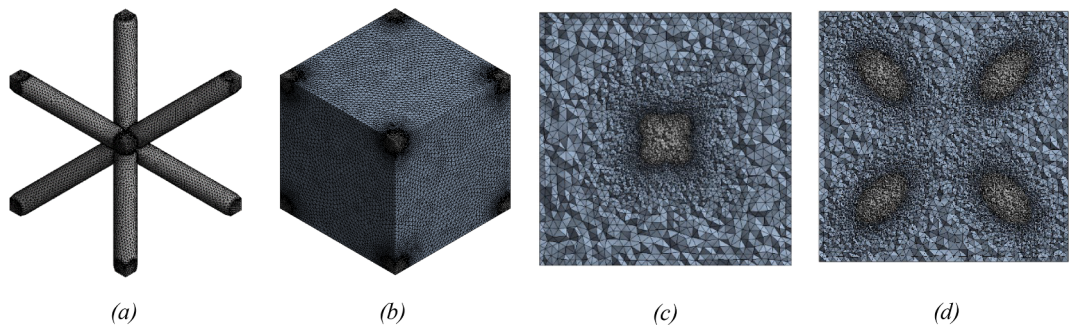


**Fig. B1.** Unstructured mesh of the unit cell with  $\varphi = 0.9$  for (a) solid phase, (b) fluid phase, (c) at  $z/L = 0.5$ , and (d) at  $z/L = 0.25$  and  $0.75$ .

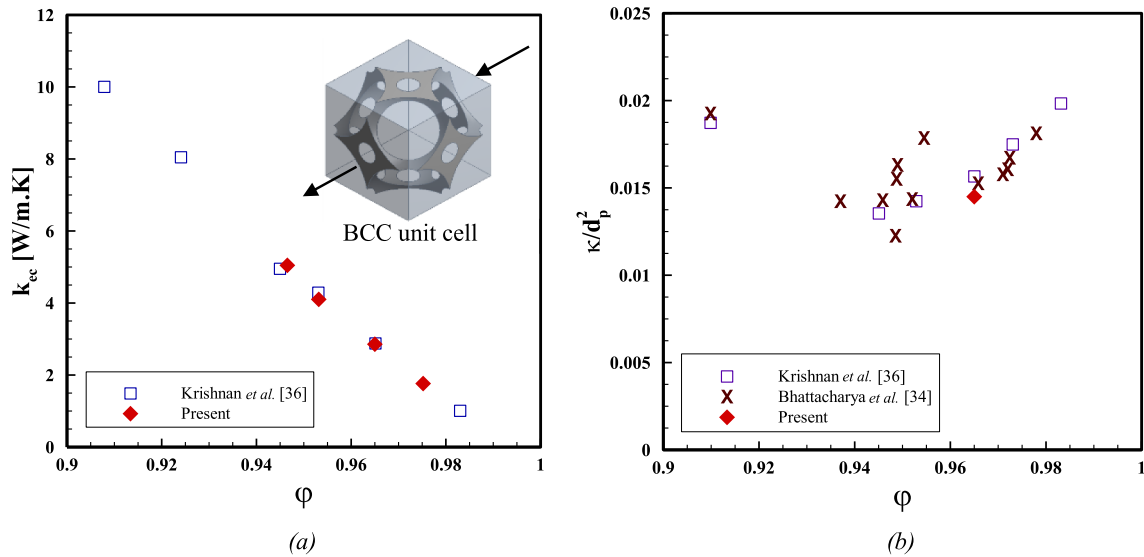


**Fig. C1.** (a) Conductive thermal conductivity and (b) Normalized permeability as a function of porosity.

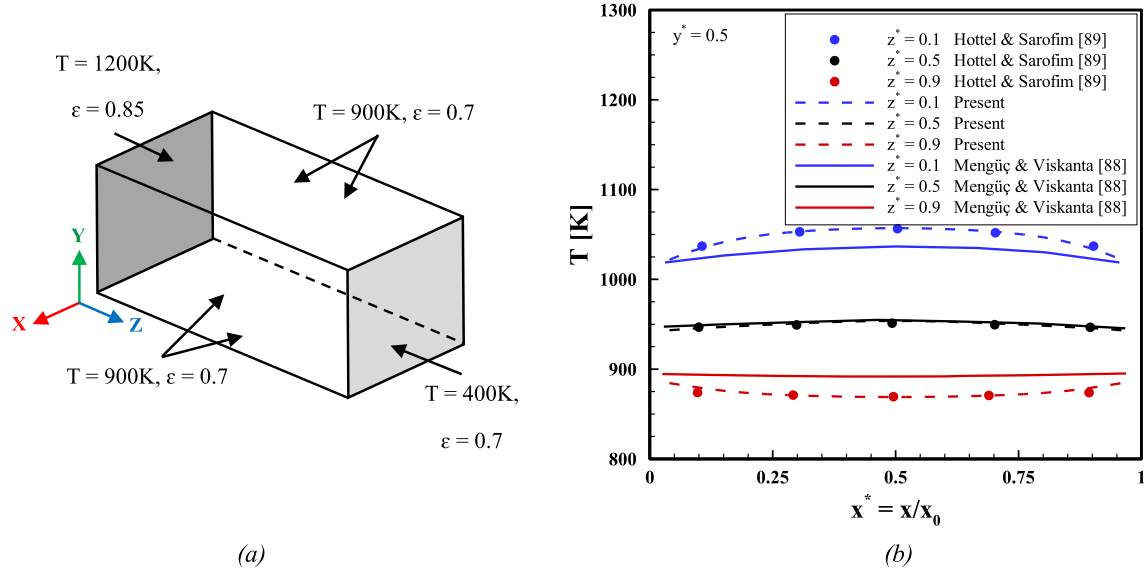


**Fig. C2.** (a) Boundary conditions and (b) Temperature distribution in the  $x$  direction along three lines at  $y^* = 0.5$  and  $z^* = 0.1, 0.5$ , and  $0.9$ .

the porosity. The numerical results show that at a constant Reynolds number, the flow velocity in the cell increases by decreasing the porosity. In a constant temperature boundary condition, the whole cell temperature increases by reducing the porosity, but it decreases for the

case of constant heat release thermal condition. Upon adding the effect of radiation heat transfer, the predicted radiative thermal conductivity shows an increase by increasing the average cell temperature, especially for higher porosities. A cubic polynomial equation in terms of the mean

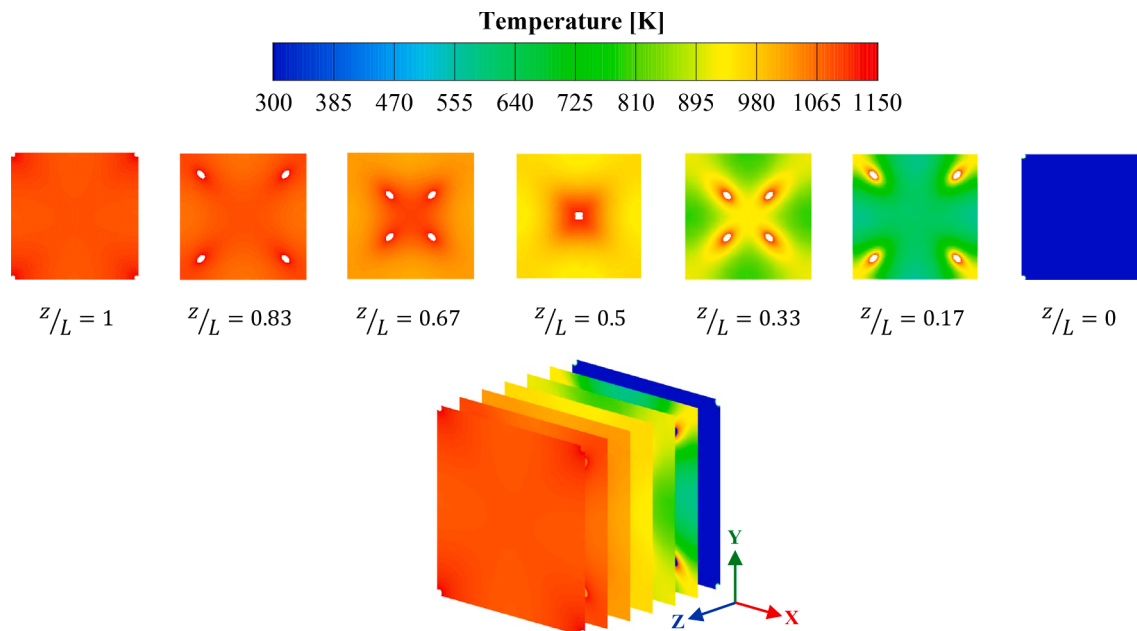


**Fig. D1.** Temperature contours of fluid at different cross-sections for BCC lattices with  $\varphi = 0.99$  and  $Re_p = 1.5625$  for constant heat release thermal condition.

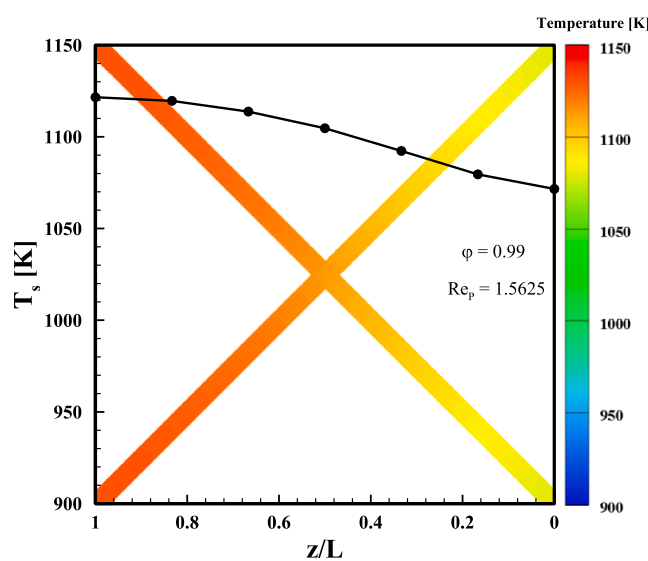


**Fig. D2.** Temperature changes of solid struts at different cross-sections for BCC lattices with  $\varphi = 0.99$  and  $Re_p = 1.5625$  for constant heat release thermal condition.

temperature correlates the radiative thermal conductivity in these geometries for the selected materials. In general, the effective thermal conductivity depends on both radiative and conductive thermal conductivities. At lower temperatures, radiative thermal conductivity is negligible compared to conductive thermal conductivity. Therefore, the effective thermal conductivity behaves similar to the conductive thermal conductivity, so it is higher at lower porosities. However, when temperature is high or the solid thermal conductivity is low, the effective thermal conductivity increases with increasing the porosity. Increasing

the cell size linearly enhances the radiative thermal conductivity. Increasing the solid radiative emission coefficient or applied temperature difference (when the average cell temperature remains constant) also leads to an incremental trend for radiative thermal conductivity. Modeling all three modes of heat transfer in the unit cells under constant heat release thermal condition shows a greater contribution of the radiative heat transfer to the total heat transfer at lower Reynolds numbers or by increasing the amount of heat release from the solid struts, an important finding of this study since radiation heat transfer is commonly neglected in lattice material design.

#### CRediT authorship contribution statement

**M. Shahrzadi:** Investigation, Formal analysis, Software, Methodology, Visualization, Writing – original draft, Writing – review & editing. **M. Davazdah Emami:** Conceptualization, Methodology, Writing – review & editing, Supervision. **A.H. Akbarzadeh:** Conceptualization, Methodology, Writing – review & editing, Supervision, Funding acquisition.

#### Declaration of Competing Interest

The authors declare that they have no known competing financial interests or personal relationships that could have appeared to influence the work reported in this paper.

#### Acknowledgements

A.H. Akbarzadeh acknowledges the financial support by Natural Sciences and Engineering Research Council of Canada through NSERC Discovery Grant RGPIN-2016-0471 and the Canada Research Chairs program in Multifunctional metamaterials. The contribution of A. Mirabolghasemi, in AM<sup>3</sup>L lab at McGill University, for the CAD modelling of lattices is acknowledged.

#### Appendix A.: Pore diameter for body-centered orthorhombic lattice

A more general case can be considered where the dimensions of 3D unit cell are not equal, a body-centered orthorhombic lattice. Assuming that the unit cell dimensions are  $a \times b \times c$  and  $a < b < c$ , three rhombus surfaces with different sizes can be considered. For each of the three closed surfaces,  $d_p$

is calculated in the same fashion as formulated in [Section 2.1](#). The diameter of the largest circle that fits the three surfaces is chosen as the equivalent pore diameter. Eqs. [\(A1\)](#) to [\(A3\)](#) present  $d_p$  based on the three rhombus surfaces:

$$\theta = \cos^{-1} \frac{\sqrt{b^2 + c^2}}{\sqrt{a^2 + b^2 + c^2}} \quad (A1)$$

$$d_p = \sqrt{b^2 + c^2} \sin \theta - d_s$$

$$\theta = \cos^{-1} \frac{\sqrt{a^2 + c^2}}{\sqrt{a^2 + b^2 + c^2}} \quad (A2)$$

$$d_p = \sqrt{a^2 + c^2} \sin \theta - d_s$$

$$\theta = \cos^{-1} \frac{\sqrt{a^2 + b^2}}{\sqrt{a^2 + b^2 + c^2}} \quad (A3)$$

$$d_p = \sqrt{a^2 + b^2} \sin \theta - d_s$$

## Appendix B.: Description of the mesh

Unstructured meshes with finer elements near the solid struts are generated for the unit cells by ANSYS Fluent meshing. [Fig. B1](#) shows the mesh for the solid phase, fluid phase, and different cross-sections in the unit cell with  $\varphi = 0.9$ . For other cases, similar mesh configurations are used.

## Appendix C.: Verification

In the first part of verification, the BCC unit cell, which has been studied by Krishnan *et al.* [\[36\]](#), is simulated. Boundary conditions are the same as those shown in [Fig. 3](#) with  $\varphi = 0.965$ ,  $Re_p = 50$ , and a constant heat flux of  $50 \text{ W/m}^2$  on the solid struts. The conductive thermal conductivity and permeability are presented in [Fig. C1](#), which shows a good agreement with the cited reference. In the second part of verification, the radiation heat transfer in a cuboid (with  $2x_0 = 2y_0 = z_0 = 4 \text{ m}$ ) is simulated, with boundary conditions as depicted in [Fig. C2a](#). The heat generation and extinction coefficient are equal to  $5 \text{ kW/m}^3$  and  $0.5 \text{ m}^{-1}$ , respectively. Results are compared to that of Mengüç & Viskanta [\[88\]](#) and Hottel & Sarofim [\[89\]](#) in [Fig. C2b](#). Temperature distribution in the x-direction at three different positions (where  $x^* = x/x_0$ ,  $y^* = y/y_0$ , and  $z^* = z/z_0$ ) are plotted in [Fig. C2b](#), which shows good agreement with the cited references.

## Appendix D.: Constant heat release thermal condition

For the constant heat release thermal condition, [Fig. D1](#) shows the temperature at different cross-sections for the  $\varphi = 0.99$  and  $Re_p = 1.5625$ , which has the highest temperature variation. In this case, due to the type of thermal condition applied, at a constant porosity, the solid struts temperature also increases from the beginning to the end of the cell. To see this more closely, [Fig. D2](#), which has a smaller temperature range, shows the solid struts temperature changes for the  $\varphi = 0.99$  and  $Re_p = 1.5625$  in terms of distance from the cell inlet. It can be seen that the closer we get to the end of the cell, fluid and solid struts become hotter.

## Appendix E.: Supplementary material

Supplementary data to this article can be found online at <https://doi.org/10.1016/j.compstruct.2021.115159>.

## References

- [1] Fleck NA, Deshpande VS, Ashby MF. Micro-architected materials: past, present and future. *Proc. R. Soc. A Math. Phys. Eng. Sci.* 2010;466(2121):2495–516.
- [2] Gibson LJ, Ashby MF, Harley BA. Cellular materials in nature and medicine. Cambridge University Press; 2010.
- [3] Nield DA, Bejan A. Convection in porous media. Springer; 2006.
- [4] Rashidi S, Kashefi MH, Kim KC, Samimi-Abianeh O. Potentials of porous materials for energy management in heat exchangers—A comprehensive review. *Appl. Energy* 2019;243:206–32.
- [5] Lebaal N, SettaR A, Roth S, Gomes S. Conjugate heat transfer analysis within in lattice-filled heat exchanger for additive manufacturing. *Mech. Adv. Mater. Struct.* 2020;1:9–9.
- [6] Pavel BI, Mohamad AA. An experimental and numerical study on heat transfer enhancement for gas heat exchangers fitted with porous media. *Int. J. Heat Mass Transf.* 2004;47(23):4939–52.
- [7] X.-H. Han, Q. Wang, Y.-G. Park, C. T'joen, A. Sommers, and A. Jacobi, “A review of metal foam and metal matrix composites for heat exchangers and heat sinks,” *Heat Transf. Eng.*, vol. 33, no. 12, pp. 991–1009, 2012.
- [8] Qiu L, Zou H, Tang D, Wen D, Feng Y, Zhang X. Inhomogeneity in pore size appreciably lowering thermal conductivity for porous thermal insulators. *Appl. Therm. Eng.* 2018;130:1004–11.
- [9] Arciniegas M, Aparicio C, Manero JM, Gil FJ. Low elastic modulus metals for joint prosthesis: Tantalum and nickel–titanium foams. *J. Eur. Ceram. Soc.* 2007;27(11):3391–8.
- [10] Mutlu I. Sinter-coating method for the production of TiN-coated titanium foam for biomedical implant applications. *Surf. Coatings Technol.* 2013;232:396–402.
- [11] Yang X, Wei P, Cui X, Jin L, He Y-L. Thermal response of annuli filled with metal foam for thermal energy storage: an experimental study. *Appl. Energy* 2019;250:1457–67.
- [12] Fuqiang W, Ziming C, Jianyu T, Jiaqi Z, Yu L, Linhua L. Energy storage efficiency analyses of CO<sub>2</sub> reforming of methane in metal foam solar thermochemical reactor. *Appl. Therm. Eng.* 2017;111:1091–100.
- [13] Tancogne-Dejean T, Spierings AB, Mohr D. Additively-manufactured metallic micro-lattice materials for high specific energy absorption under static and dynamic loading. *Acta Mater.* 2016;116:14–28.
- [14] Rashidi S, Esfahani JA, Rashidi A. A review on the applications of porous materials in solar energy systems. *Renew. Sustain. Energy Rev.* 2017;73:1198–210.
- [15] Hohe J, et al. Numerical and experimental design of graded cellular sandwich cores for multi-functional aerospace applications. *Mater. Des.* 2012;39:20–32.
- [16] García-Moreno F. Commercial applications of metal foams: Their properties and production. *Materials (Basel)* 2016;9(2):85.
- [17] Zinno A, Fusco E, Prota A, Manfredi G. Multiscale approach for the design of composite sandwich structures for train application. *Compos. Struct.* 2010;92(9):2208–19.

- [18] Shi J, Mofatteh H, Mirabolghasemi A, Desharnais G, Akbarzadeh A. Programmable Multistable Perforated Shellular. *Adv. Mater.* 2021;21:202423.
- [19] De Lemos MJS. *Turbulence in porous media: modeling and applications*. Elsevier; 2012.
- [20] Dybbs A, Edwards RV. “A new look at porous media fluid mechanics—Darcy to turbulent. In: *Fundamentals of transport phenomena in porous media*. Dordrecht: Springer; 1984. p. 199–256.
- [21] Darcy H. *Les fontaines publiques de la ville de Dijon: exposition et application*. Victor Dalmont; 1856.
- [22] Boomsma K, Poulikakos D, Ventikos Y. Simulations of flow through open cell metal foams using an idealized periodic cell structure. *Int. J. Heat Fluid Flow* 2003;24(6): 825–34.
- [23] Wu Z, et al. Experimental and numerical studies of the pressure drop in ceramic foams for volumetric solar receiver applications. *Appl. Energy* 2010;87(2):504–13.
- [24] Otaru AJ, Morvan HP, Kennedy AR. Measurement and simulation of pressure drop across different porous aluminium in the Darcy-Forchheimer regime. *Acta Mater.* 2018;149:265–73.
- [25] Xu W, Zhang H, Yang Z, Zhang J. Numerical investigation on the flow characteristics and permeability of three-dimensional reticulated foam materials. *Chem. Eng. J.* 2008;140(1–3):562–9.
- [26] Weber L, Ingram D, Guardia S, Athanasiou-Ioannou A, Mortensen A. Fluid flow through replicated microcellular materials in the Darcy-Forchheimer regime. *Acta Mater.* 2017;126:280–93.
- [27] Nickerson S, Shu Y, Zhong D, Konke C, Tandia A. Permeability of porous ceramics by X-ray CT image analysis. *Acta Mater.* 2019;172:121–30.
- [28] Lee O-J, Lee K-H, Yim TJ, Kim SY, Yoo K-P. Determination of mesopore size of aerogels from thermal conductivity measurements. *J. Non. Cryst. Solids* 2002;298 (2–3):287–92.
- [29] Hrubesh LW, Pekala RW. Thermal properties of organic and inorganic aerogels. *J. Mater. Res.* 1994;9(3):731–8.
- [30] Solorzano E, Rodriguez-Perez MA, Lázaro J, de Saja JA. Influence of solid phase conductivity and cellular structure on the heat transfer mechanisms of cellular materials: diverse case studies. *Adv. Eng. Mater.* 2009;11(10):818–24.
- [31] Calmudi VV, Mahajan RL. The Effective Thermal Conductivity of High Porosity Fibrous Metal Foams. *J. Heat Transfer* 1999;121(2):466.
- [32] Paek JW, Kang BH, Kim SY, Hyun JM. Effective Thermal Conductivity and Permeability of Aluminum Foam Materials. *Int. J. Thermophys.* 2000;21(2): 453–64.
- [33] Boomsma K, Poulikakos D. On the effective thermal conductivity of a three-dimensionally structured fluid-saturated metal foam. *Int. J. Heat Mass Transf.* 2001;44(4):827–36.
- [34] Bhattacharya A, Calmudi VV, Mahajan RL. Thermophysical properties of high porosity metal foams. *Int. J. Heat Mass Transf.* 2002;45(5):1017–31.
- [35] Chan KC, Tso CY, Hussain A, Chao CYH. A theoretical model for the effective thermal conductivity of graphene coated metal foams. *Appl. Therm. Eng.* 2019; 161:114112.
- [36] Krishnan S, Murthy JY, Garimella SV. Direct Simulation of Transport in Open-Cell Metal Foam. *J. Heat Transfer* 2006;128(8):793–9.
- [37] Wang G, Wei G, Xu C, Ju X, Yang Y, Du X. Numerical simulation of effective thermal conductivity and pore-scale melting process of PCMs in foam metals. *Appl. Therm. Eng.* 2019;147:464–72.
- [38] Yang H, Li Y, Yang Y, Chen D, Zhu Y. Effective thermal conductivity of high porosity open-cell metal foams. *Int. J. Heat Mass Transf.* 2020;147:118974.
- [39] Mirabolghasemi A, Akbarzadeh AH, Rodrigue D, Therriault D. Thermal conductivity of architected cellular metamaterials. *Acta Mater.* 2019;174:61–80.
- [40] Hou X, Zhang R, Fang D. An ultralight silica-modified ZrO<sub>2</sub>–SiO<sub>2</sub> aerogel composite with ultra-low thermal conductivity and enhanced mechanical strength. *Scri. Mater.* 2018;143:113–6.
- [41] Singh R, Kasana HS. Computational aspects of effective thermal conductivity of highly porous metal foams. *Appl. Therm. Eng.* 2004;24(13):1841–9.
- [42] Ranut P. On the effective thermal conductivity of aluminum metal foams: Review and improvement of the available empirical and analytical models. *Appl. Therm. Eng.* 2016;101:496–524.
- [43] Shirvan KM, Ellahi R, Mirzakhanlari S, Mamourian M. Enhancement of heat transfer and heat exchanger effectiveness in a double pipe heat exchanger filled with porous media: numerical simulation and sensitivity analysis of turbulent fluid flow. *Appl. Therm. Eng.* 2016;109:761–74.
- [44] Mohammadi MH, Abbasi HR, Yavarinasab A, Pourrahmani H. Thermal optimization of shell and tube heat exchanger using porous baffles. *Appl. Therm. Eng.* 2020;170:115005.
- [45] Buonomo B, di Pasqua A, Manca O, Nardini S. Evaluation of thermal and fluid dynamic performance parameters in aluminum foam compact heat exchangers. *Appl. Therm. Eng.* 2020;115456.
- [46] Son KN, Weibel JA, Kumaresan V, Garimella SV. Design of multifunctional lattice-frame materials for compact heat exchangers. *Int. J. Heat Mass Transf.* 2017;115: 619–29.
- [47] Zafari M, Panjepour M, Emami MD, Meratian M. Microtomography-based numerical simulation of fluid flow and heat transfer in open cell metal foams. *Appl. Therm. Eng.* 2015;80:347–54.
- [48] Du S, Tong Z-X, Zhang H-H, He Y-L. Tomography-based determination of Nusselt number correlation for the porous volumetric solar receiver with different geometrical parameters. *Renew. Energy* 2019;135:711–8.
- [49] Jafarizadeh A, Panjepour M, Meratian M, Emami MD. Numerical simulation of gas/ solid heat transfer in metallic foams: A general correlation for different porosities and pore sizes. *Transp. porous media* 2019;127(2):481–506.
- [50] Yan H, Zhang Q, Chen W, Xie G, Dang J, Lu TJ. An X-lattice cored rectangular honeycomb with enhanced convective heat transfer performance. *Appl. Therm. Eng.* 2020;166:114687.
- [51] Ma Y, Yan H, Xie G. Flow and thermal performance of sandwich panels with plate fins or/and pyramidal lattice. *Appl. Therm. Eng.* 2020;164:114468.
- [52] Krishnan S, Garimella SV, Murthy JY. Simulation of Thermal Transport in Open-Cell Metal Foams: Effect of Periodic Unit-Cell Structure. *J. Heat Transfer* 2008;130 (2):024503.
- [53] Yang G, Hou C, Zhao M, Mao W. Comparison of convective heat transfer for Kagome and tetrahedral truss-cored lattice sandwich panels. *Sci. Rep.* 2019;9(1): 1–13.
- [54] Shen B, Yan H, Xue H, Xie G. The effects of geometrical topology on fluid flow and thermal performance in Kagome cored sandwich panels. *Appl. Therm. Eng.* 2018; 142:79–88.
- [55] Jin X, Shen B, Yan H, Sunden B, Xie G. Comparative evaluations of thermofluidic characteristics of sandwich panels with X-lattice and Pyramidal-lattice cores. *Int. J. Heat Mass Transf.* 2018;127:268–82.
- [56] S. Cunsolo, M. Iasiello, M. Oliviero, N. Bianco, W. K. S. Chiu, and V. Naso, “Lord Kelvin and Weaire-Phelan foam models: Heat transfer and pressure drop,” *J. Heat Transfer*, vol. 138, no. 2, 2016.
- [57] Kaur I, Singh P. Endwall heat transfer characteristics of octahedron family lattice-frame materials. *Int. Commun. Heat Mass Transf.* 2021;127:105522.
- [58] Liang D, Bai W, Chen W, Chyu MK. Investigating the effect of element shape of the face-centered cubic lattice structure on the flow and endwall heat transfer characteristics in a rectangular channel. *Int. J. Heat Mass Transf.* 2020;153: 119579.
- [59] Du S, Li M-J, Ren Q, Liang Q, He Y-L. Pore-scale numerical simulation of fully coupled heat transfer process in porous volumetric solar receiver. *Energy* 2017; 140:1267–75.
- [60] Peng Q, et al. Experimental investigation on premixed hydrogen/air combustion in varied size combustors inserted with porous medium for thermophovoltaic system applications. *Energy Convers. Manag.* 2019;200:112086.
- [61] Zhao CY, Tassou SA, Lu TJ. Analytical considerations of thermal radiation in cellular metal foams with open cells. *Int. J. Heat Mass Transf.* 2008;51(3–4): 929–40.
- [62] Coquard R, Rochais D, Baillis D. Conductive and radiative heat transfer in ceramic and metal foams at fire temperatures. *Fire Technol.* 2012;48(3):699–732.
- [63] Patel VM, Mendes MAA, Talukdar P, Ray S. Development of correlations for effective thermal conductivity of a tetrakaidecahedra structure in presence of combined conduction and radiation heat transfer. *Int. J. Heat Mass Transf.* 2018; 127:843–56.
- [64] Patel VM, Talukdar P. Determination of radiative properties of representative and real open cell foam structures using the finite volume method. *Int. J. Therm. Sci.* 2018;132:117–28.
- [65] Pelanconi M, Barbato M, Zavattone S, Vignoles GL, Ortona A. Thermal design, optimization and additive manufacturing of ceramic regular structures to maximize the radiative heat transfer. *Mater. Des.* 2019;163:107539.
- [66] Ali M, Rady M, Attia MAA, Ewais EMM. Consistent coupled optical and thermal analysis of volumetric solar receivers with honeycomb absorbers. *Renew. Energy* 2020;145:1849–61.
- [67] Li Z, Xia X, Li X, Sun C. Discrete vs. continuum-scale simulation of coupled radiation and convection inside rectangular channel filled with metal foam. *Int. J. Therm. Sci.* 2018;132:219–33.
- [68] Lee J, Song T-H. Conduction/radiation combined heat transfer with contact resistance for application to vacuum insulation. *Int. J. Heat Mass Transf.* 2019;129: 380–8.
- [69] Yang Z, Wang Z, Yang Z, Sun Y. Multiscale analysis and computation for coupled conduction, convection and radiation heat transfer problem in porous materials. *Appl. Math. Comput.* 2018;326:56–74.
- [70] Jang D, Meza LR, Greer F, Greer JR. Fabrication and deformation of three-dimensional hollow ceramic nanostructures. *Nat. Mater.* 2013;12(10):893–8.
- [71] Vyatskikh A, Delalande S, Kudo A, Zhang X, Portela CM, Greer JR. Additive manufacturing of 3D nano-architected metals. *Nat. Commun.* 2018;9(1):1–8.
- [72] Ngo TD, Kashani A, Imbalzano G, Nguyen KTQ, Hui D. Additive manufacturing (3D printing): A review of materials, methods, applications and challenges. *Compos. Part B Eng.* 2018;143:172–96.
- [73] Shi J, Akbarzadeh AH. Architected cellular piezoelectric metamaterials: Thermo-electro-mechanical properties. *Acta Mater.* 2019;163:91–121.
- [74] Shi J, Akbarzadeh AH. 3D Hierarchical lattice ferroelectric metamaterials. *Int. J. Eng. Sci.* 2020;149:103247.
- [75] Babae S, Shim J, Weaver JC, Chen ER, Patel N, Bertoldi K. 3D soft metamaterials with negative Poisson's ratio. *Adv. Mater.* 2013;25(36):5044–9.
- [76] Al-Ketan O, Rowshan R. The effect of architecture on the mechanical properties of cellular structures based on the IWP minimal surface. *J. Mater. Res.* 2018;33(3): 343–59.
- [77] Sarvestani HY, Akbarzadeh AH, Mirbolghasemi A, Hermenean K. 3D printed meta-sandwich structures: Failure mechanism, energy absorption and multi-hit capability. *Mater. Des.* 2018;160:179–93.
- [78] Yin H, Liu Z, Dai J, Wen G, Zhang C. Crushing behavior and optimization of sheet-based 3D periodic cellular structures. *Compos. Part B Eng.* 2020;182:107565.
- [79] Benedetti M, Du Plessis A, Ritchie RO, Dallago M, Razavi SMJ, Berto F. Architected cellular materials: A review on their mechanical properties towards fatigue-tolerant design and fabrication. *Mater. Sci. Eng. R Reports* 2021;144:100606.
- [80] Bai L, et al. Influence of unit cell pose on the mechanical properties of Ti6Al4V lattice structures manufactured by selective laser melting. *Addit. Manuf.* 2020;34: 101222.

- [81] Maconachie T, et al. SLM lattice structures: Properties, performance, applications and challenges. *Mater. Des.* 2019;183:108137.
- [82] Liu Y, Dong Z, Ge J, Lin X, Liang J. Stiffness design of a multilayer arbitrary BCC lattice structure with face sheets. *Compos. Struct.* 2019;230:111485.
- [83] Tancogne-Dejean T, Mohr D. Stiffness and specific energy absorption of additively-manufactured metallic BCC metamaterials composed of tapered beams. *Int. J. Mech. Sci.* 2018;141:101–16.
- [84] Peng C, Tran P, Nguyen-Xuan H, Ferreira AJM. Mechanical performance and fatigue life prediction of lattice structures: Parametric computational approach. *Compos. Struct.* 2020;235:111821.
- [85] Naing MW, Chua CK, Leong KF, Wang Y. Fabrication of customised scaffolds using computer-aided design and rapid prototyping techniques. *Rapid Prototyp. J.* 2005;11(4):249–59.
- [86] Bird RB, Stewart WE, Lightfoot EN. *Transport phenomena*, vol. 1. John Wiley & Sons; 2006.
- [87] Fluent A. *Theory Guide 17.2*. USA: Ansys Inc; 2016.
- [88] Mengüç MP, Viskanta R. Radiative transfer in three-dimensional rectangular enclosures containing inhomogeneous, anisotropically scattering media. *J. Quant. Spectrosc. Radiat. Transf.* 1985;33(6):533–49.
- [89] Hottel HC, Sarofim AF. *Radiative transfer*. New York: McGraw-Hill; 1967.
- [90] Beavers GS, Sparrow EM. Non-Darcy flow through fibrous porous media. *J. Appl. Mech.* 1969;711–4.
- [91] Vafai K, Tien CL. Boundary and inertia effects on convective mass transfer in porous media. *Int. J. Heat Mass Transf.* 1982;25(8):1183–90.